

¹ **Complicated reflection of linear internal tides from the Tasman continental**

² **slope**

³ **JODY M. KLYMAK, ***

The University of Victoria, Victoria, Canada

⁴ **Harper L. Simmons and Dmitry Braznikov**

Affiliation, City, State/Province, Country

⁵ **Samuel Kelly**

Affiliation, City, State/Province, Country

⁶ **Jennifer A. MacKinnon, Matthew H. Alford, and Robert Pinkel**

Affiliation, City, State/Province, Country

⁷ **Jonathan D. Nash**

Affiliation, City, State/Province, Country

* Corresponding author address: Jody Klymak, University of Victoria, Victoria, BC, Canada

E-mail: jklymak@uvic.ca

ABSTRACT

9 The reflection of a low-mode incident internal tide on the Tasman continental slope is investigated using
10 simulations of both the real topography, and simplified topographies. The majority of the slope is super-
11 critical to the internal tide, but the response to the slope is complicated by a number of factors. The
12 incoming beam is confined in space, it impacts the slope at an angle, there is a roughly cylindrical rise
13 directly offshore of the slope, and a slope-mode wave is excited. These effects are isolated in simulations that
14 significantly simplify the topography. Determining a reflected signal from an incident one is non-trivial, even
15 in a numerical model, and the technique used here is to remove the reflector from the simulation and subtract
16 an incident response from the total response to arrive at a reflected signal. Overall, the real slope reflects
17 approximately 65% of the mode-1 internal tide as a mode-1 signal, which is less than two-dimensional linear
18 calculations would predict, likely due to three-dimensional concavity of the topography. It is also less than
19 recent glider estimates due to along-slope inhomogeneity. A synthetic three-point mooring array can predict
20 almost any reflectivity because of spatial inhomogeneity. The Tasman Rise serves to diffract the incoming
21 tidal beam into two beams, one focused downstream, and one diffracted to the north, with a substantial
22 null in incoming energy between them. Along-slope heterogeneity is further enhanced by a partially trapped
23 super-inertial slope wave that propagates along the continental slope, removing energy from the internal
24 tide in some spots and re-radiating it further north. This wave is present even in a simplified straight-shelf
25 topography.

²⁶ 1. Introduction

²⁷ Energy is lost from the surface tide when it interacts with topography, and in the deep ocean is largely
²⁸ redistributed as an internal tide. The fate of the internal tide is unclear, but surely depends on the dominant
²⁹ wavelengths that are forced. Gentle topography that is subcritical to the internal tide is likely dominated by
³⁰ higher vertical modes and is thought to break via wave-wave interactions relatively close to the topography
³¹ (i.e. Polzin 2009; St. Laurent and Garrett 2002). However, steeper supercritical topography, while exhibiting
³² significant local dissipation, tends to radiate a large fraction of the internal tide away from the topography as
³³ low-mode waves (i.e. at Hawaii Klymak et al. 2006; Carter et al. 2008). Given that a significant fraction of
³⁴ the internal tide energy is generated at steep topography (Legg and Klymak 2008), and that the distribution
³⁵ of the mixing it eventually drives has impacts on understanding the distribution of ocean properties and the
³⁶ strength of the overturning circulation (i.e. Melet et al. 2013), it is desirable to understand where and how
³⁷ this energy breaks.

One candidate sink for the low-mode internal tide is reflection and scattering from continental slopes. These slopes are known to be hotspots of turbulent mixing from the few observational studies to date (Nash et al. 2007; Klymak et al. 2011; Martini et al. 2013). However, these studies have also demonstrated some of the difficulties in tracking internal tide energy on these slopes. Net internal-tide fluxes are relatively straight forward to measure, but ideally we would like to separate the incident and reflected fluxes if a parameterization of turbulence on the slope is to be made since the incident fluxes are what drive the turbulence. The reflectivity of a continental slope is basically the ratio of the energy flux convergence divided by the total incident flux:

$$R = \frac{F_{out}}{F_{in}},$$

³⁸ where F is depth integrated for a two-dimensional budget or line-integrated for a three-dimensional one.
³⁹ Even simple two-dimensional linear models of reflection indicate that determining the reflectivity will be
⁴⁰ challenging, with reflection co-efficients strongly depending on the modal content and phases of the incident
⁴¹ internal tides (Klymak et al. 2011) and the local surface tide (Kelly and Nash 2010). These linear models
⁴² have been used globally to estimate reflection co-efficients for the mode-1 tides on realistic continental slope
⁴³ bathymetries, (Kelly et al. 2013a,b), but these calculations assume the incoming tide is known, and that the
⁴⁴ slope is relatively homogenous over a long distance (presumably the mode-1 wavelength).

⁴⁵ Determining the incident flux, F_{in} , from field data, and even from a numerical model with sufficient
⁴⁶ complexity, is not trivial. In two dimensions, or with simple plane wave geometries, it is relatively easy to
⁴⁷ fit incident and reflected plane waves and recover the desired reflection co-efficient (figure 1a). In the real
⁴⁸ ocean, even if the tidal components can be easily separated from confounding influences, internal tides are

49 often spatially inhomogeneous, and form lateral “beams” (in x-y) that make plane wave fits difficult from a
50 finite array of moorings; for instance the mooring array could be located more in the incoming beam than
51 the reflected, leading to an exaggeration of the dissipation (figure 1b). Plane-wave fits to satellite altimetry
52 tracks are promising, but will also suffer from a lack of fidelity if the internal tides are inhomogeneous on
53 the scale of the plane wave fits (Zhao and Alford 2009). In the model, high resolution temporal and spatial
54 information makes it possible to separate signals spectrally according to their direction of propagation (i.e.
55 using a Hilbert transform Mercier et al. 2008), but this method works best if there are no boundaries and the
56 signals at the edges of the model domain can be tapered to reduce leakage, neither of which are applicable
57 here.

58 The region considered here is the Tasman continental slope, and is the focus of a concentrated internal
59 tide experiment. As preliminary work, it has been sampled continuously by gliders for many months in 2012
60 and 2013 (Johnston et al. 2015). The gliders were flown to form internal waves antennae over which internal
61 plane-wave fits were made. These efforts show a clear standing wave pattern, with amplitudes and phases
62 as one would expect for internal waves incident on the slope from the southeast where internal tides are
63 expected to be generated from the Macquarie Ridge (figure 2a). The amplitudes of the interfering waves
64 were such that the reflectivity is predicted to be high on this slope, with estimates of 0.7 to 1. from the
65 arrays (Johnston et al. 2015). The gliders also picked up a 100-km wavelength wave propagating along slope
66 towards the north, a finding we isolate and discuss below.

67 Here we run numerical simulations that are meant to represent a mode-1 internal M_2 tide incident on
68 the Tasman Slope, east of Tasmania. The simulations are only forced by this incident internal tide, and
69 there is no local forcing, allowing the effect of the reflection to be isolated. After discussing the model setup
70 section 2, we briefly consider the response this forcing has on the slope section 3 and compute and energy
71 budget of the complete response. In order to separate the physics of the reflection, we then simplify the
72 geometry section 4, both geometrically, and by removing parts of the topography. This technique allows us
73 to separate incident and reflected signals from the total response without appeal to simplified wavefits. We
74 end with a discussion of the results (section 5) and a summary (section 6).

75 2. Model setup

76 a. Basics

77 The numerical model used here is the MITGCM (Marshall et al. 2006). The setup is very similar
78 to Buijsman et al. (2014), with the model run in hydrostatic mode, background (isotropic) diffusivities

79 and viscosities of $10^{-5} \text{ m}^2 \text{s}^{-1}$, and enhanced diffusivity and viscosity in regions of temporarily unstable
 80 stratification, as in Klymak and Legg (2010). A second-order flux-limiting temperature advection scheme
 81 is used which results in some numerical dissipation and diffusion. Tests were run with weaker forcing, and
 82 the fraction of energy dissipated did not change, indicating that the dissipation highlighted below is heavily
 83 influenced by numerical dissipation due to the lack of lateral resolution. Dissipation is not the main focus
 84 of this paper, and finer resolutions have been used for more focused efforts dealing with turbulence on the
 85 slope.

86 Topography is from a data set that combines Smith and Sandwell (1997) and multibeam data from
 87 Australian surveys (Whiteway 2009) (figure 2b). For this paper, we use a cartesian co-ordinate system
 88 centered at 44S, 148 E, with y pointing 12 degrees east of geographic north (magenta lines figure 2). This
 89 co-ordinate system is close to cross-slope in the x-direction, and is used for conceptual convenience. The
 90 simulations are run on a f-plane ($f = -10^{-4} \text{ s}^{-1}$), so no planetary beta effect has been included.

91 Relatively high lateral resolution is used along the continental slope (figure 3a, smallest inset green box)
 92 of $\delta x = \delta y = 1 \text{ km}$. Resolution is expanded by 3.5% per grid cell beyond the high-resolution region, to a
 93 maximum of 5 km in the second largest inset box (figure 3a); this keeps the resolution over the Tasman Rise
 94 and the rest of the continental slope at least 5 km. Further out, the grid spacing is again increased at 3.5%
 95 per grid cell until a maximum grid cell size of 10 km is reached.

96 Vertical resolution is approximately stretched so $dz \sim N$, where $N^2(z) = -\frac{g}{\rho_0} \frac{d\rho}{dz}$ is the vertical stratifi-
 97 cation. 200 vertical grid cells are used for these simulations. The vertical stratification is from the World
 98 Ocean Atlas for the Tasman Sea just offshore of Tasmania (Boyer et al. 2013), and is assumed laterally
 99 constant in the domain. This precludes any mesoscale effects, which are believed to be important in this
 100 area, and are the subject of future work.

101 b. Forcing

102 To simplify the generation problem we apply an analytical forcing to our model. This is composed of
 103 two line sources at approximately the location of the Macquarie Ridge (figure 3a). The initial conditions
 104 and the southern and eastern boundaries of the model were set with this forcing. The forcing is based on
 105 (Rainville et al. 2010), except instead of a single point source placed a distance R from the line source, the
 106 line source is digitized as a number of discrete point sources and their response in the domain summed. The
 107 mode-1 pressure anomaly is given by:

$$108 p'(x, y, t) = \sum_{i=1}^N a_i \exp(j(|k_t|r_i - \omega t)) \quad (1)$$

108 where $r_i = \sqrt{(x - x_i)^2 + (y - y_i)^2}$ is the distance to the source, and $|k_t|$ is the absolute value of the mode-1
 109 wavenumber:

$$k_t = \frac{(\omega^2 - f^2)^{1/2}}{c_e} \quad (2)$$

110 where ω is the frequency of the tide, f is the Coriolis frequency, and c_e is the eigenspeed of the vertical mode
 111 equation:

$$\frac{d}{dz} \left(\frac{1}{N^2} \frac{d\psi}{dz} \right) + \frac{1}{c_e^2} \psi(z) = 0. \quad (3)$$

112 Here $\psi(z)$ is the eigenfunction that sets the shape of the vertical mode, and the boundary conditions are
 113 $d\psi/dz = 0$ at $z = 0$ and $z = -H$, where H is the water depth. For convenience, we normalize $\psi_m(z)$ so that

$$\int_{-H}^0 \psi_m^2(z) dz = 1. \quad (4)$$

114 Horizontal velocities can be linearly decomposed by these shapes, as can the pressure signal; vertical veloci-
 115 ties, and displacements are decomposed by the derivative of the normalized ψ_m : $d\psi_m/dz$.

116 To compute the wavefield, the horizontal velocity components are derived from the internal wave consis-
 117 tency relations:

$$u(x, y, t) = \sum_{i=1}^N \frac{k_x \omega + j k_y f}{\omega^2 - f^2} \frac{p'_i}{\rho} \quad (5)$$

$$v(x, y, t) = \sum_{i=1}^N \frac{k_y \omega - j k_x f}{\omega^2 - f^2} \frac{p'_i}{\rho} \quad (6)$$

118 where $k_x = k_t \cos(\theta_i)$ and $k_y = k_t \sin(\theta_i)$ are calculated from the angle to each element of the line sources
 119 $\theta_i = \arctan((y - y_i)/(x - x_i))$.

120 The resulting incoming wavefield (figure 3a) has a beam of energy flux that radiates northwest, and is
 121 relatively tightly focused. The interference pattern creates a null to the south and north, and a secondary
 122 beam that radiates due west. This schematic agrees with more realistic regional tidal models (H. Simmons,
 123 in preparation), and the amplitude of the beam was tuned to give approximately 7 kW m^{-1} of flux incident
 124 at Tasmania in the pictured realization. Most runs below were scaled to have weaker (more linear) fluxes,
 125 with approximately 2 kW m^{-1} at Tasmania, but exactly the same spatial pattern. The initial condition is
 126 applied uniformly through the domain, regardless of bathymetry, so there are some start-up transients as
 127 the proper baroclinic flow develops.

128 This forcing is applied on the eastern and southern boundaries of the domain. The northern and western
 129 boundaries are sponges where the velocity is slowly dropped to zero and the stratification relaxed to the
 130 initial stratification (figure 3a, green rectangles). Our main focus is the area from $y=0$ to 400 km, so the
 131 boundaries are sufficiently far that small residual reflections do not affect the response.

132 The ideal response off the Tasman topography would be as a plane-wave reflection from a wall at $x = 0$ km
133 (i.e. Johnston et al. 2015). Here we have a relatively confined beam, but we can make a start by considering
134 the reflection the beam from a wall at $x = 0$ km for $y > 0$ km (figure 3b,c) using the method of images
135 with identical line sources mirrored about the y-axis, and their phase shifted by 180 deg. The reflection
136 pattern that sets up is not entirely regular, but has some straight-forward features. The incoming beam
137 impacts the wall at approximately 30 deg. The horizontal wavelength of an M_2 internal tide is 178 km, so
138 the standing wave in the x-direction will have a wavelength $178/\cos(30) \approx 200$ km and in the y-direction
139 will have a wavelength of approximately 350 km. These spatial scales are readily apparent in the analytical
140 forcing despite the non-plane-wave character of the idealized forcing (figure 3c). Note that the standing
141 energy flux (figure 3b) has peaks and nulls in absolute value, with the peaks having large flux to the north.
142 The peaks are every half cross-slope wavelength (i.e. 100 km). The nulls have weak southward energy flux
143 (though it is difficult to discern from the subsampled arrows in the plot).

144 3. Realistic model simulation

145 The response of the forcing in the most complex domain motivates the more idealized experiments that
146 follow. From the initial forcing (figure 4a), a complex wavefield develops with clear scattering from the
147 Tasman Rise, the shelf, and numerous small inhomogeneities on the sea floor (figure 4b-d). Looking along
148 shelf, the phase of the velocity signal can be seen changing approximately every 200 km, and it changes
149 approximately every 100 km offshelf.

150 This sets up a complicated interference pattern that shows inconsistent cross-slope fluxes and peaks and
151 nulls in the along-slope fluxes to the north, as we might expect from an oblique standing wave (compare
152 figure 4h to figure 3b). However the pattern is complicated, with offshore peaks at approximately the correct
153 spacing offshore, but not lining up precisely in the north-south direction. There are inhomogeneities in the
154 energy that are not accounted for by a simple two-wave model.

155 An energy balance is performed on the model using the terms outlined in Kang and Fringer (2012); Kang
156 (2011). Their energy balance vertically integrated can be schematicized as:

$$dE_{bc}/dt = -\nabla_H \mathbf{F}_{bc} + \text{Conversion} - \text{Dissipation}. \quad (7)$$

157 where E_{bc} is the depth-integrated baroclinic energy density, \mathbf{F}_{bc} is the depth integrated energy flux, including
158 both the pressure work term and the non-linear advection of energy (which is small in our runs). “Conver-
159 sion” is a complex term representing transfer from barotropic motions to baroclinic (Kang 2011, eq. 5.102)
160 and includes the barotropic heaving of the water column, the density anomaly, and a non-linear horizontal

advection term. The non-linear terms can be non-trivial in real bathymetry (Buijsman et al. 2014). The conversion term is positive if the barotropic tide loses energy and the baroclinic tide gains energy. “Dissipation” is computed here as the residual, and includes dissipation due to interior viscosity, numerical dissipation, bottom drag, and diffusion of energy (small).

Of note in the energy calculation is that the largest local term in the energy budget is an alternating pattern of barotropic-baroclinic conversion at the shelf break balanced by baroclinic flux convergences and divergences (figure 5). The importance of the barotropic-baroclinic term can also be seen by considering the x-integral of the energy budget from $x = -50$ km to +100 km (figure 6). Recall that the simulations have no barotropic forcing. This coupling is catalyzed by a start-up transient hitting the slope with the incoming internal tide beam, and continues throughout the simulation, and is probably a leaky super-inertial slope wave (see section 5).

The time series of the energy terms integrated along the shelf demonstrates that the barotropic-to-baroclinic term is relatively small when averaged, with a small loss of energy from the baroclinic tide to the barotropic in the integral region (figure 6b). The model is largely in a steady state by tidal cycle 15, with some residual oscillations in dE/dt and the flux convergence. The large-scale baroclinic energy changes do not change the dissipation residual very much, which is relatively constant after 5 tidal cycles. To put the 50 MW of dissipation into context, the initial energy that comes in the east and south sides of this analysis box in the initial conditions is 315 MW, so the model is dissipating about 17% of the incoming energy. However, note that the dissipation is not the focus of these model runs nor of this paper. The forcing here is approximately a factor 3 lower than the real forcing, so its likely the fraction of dissipation at this site is higher (probably closer to 25%) if real forcing is used.

The majority of the energy budget is in the first vertical mode (figure 6c). Net fluxes in the region directly offshore of the shelf break ($0 < x < 80$ km, and $0 < y < 400$ km) are composed of substantial mode-1 energy converging on the shelf (95 MW net), and some reflected energy escaping in higher modes (28.3 MW, mostly in modes 2–4). The 95 MW net flux is made up of the incoming and reflected mode-1 energy, and separating those fractions out is the subject of the next section. There is some incoming higher-mode energy as well due to scattering from the Tasman Rise, but as we will also show below, this is minor. The spatial pattern (not shown) of the mode conversion at the continental slope indicates hot-spots for conversion. Modes 2 and 4 have a hotspot of conversion near $y = 250$ km, and Mode 3 at $y = 325$ km.

190 4. Simplified geometries

191 To help tease apart the effects of the Tasman Rise and the non-uniform shelf, we carry out a few simplified
 192 geometric experiments (figure 7;figure 8). The REAL case is the one discussed above (figure 8f). The NO
 193 TOPO case has no topography at all (figure 8a), just the beam being forced at the south and east boundaries
 194 and (mostly) absorbed at the west and north. RISE was run with the real bathymetry west of $x = 70$ km
 195 (figure 8e). Three idealized geometries simplify the physics even more: the SHELF case has a supercritical
 196 two-dimensional continental shelf running north from $y = 0$ km(figure 8d). ROUND RISE is a 1700-m tall
 197 cylinder-shaped bump with radius of 50 km centered at approximately the same location as the Tasman Rise,
 198 with no shelf to the west (figure 8b). The simplified shelf and the rise are both used in the SHELF/RISE case
 199 (figure 8c).

200 a. Shelf-only configuration

201 The simplest topography is the SHELF configuration (figure 8d). Here we have a response that is quite
 202 similar to the analytical response calculated above (figure 3b). The only difference between these two cases
 203 is the narrow shelf west of $x = 0$ km and the slight slope to the continental slope. The interference pattern
 204 between the incoming wave and the reflected wave is clear in this plot, with the same characteristic length
 205 scales as above, and a slight bending of the response due to the radial spreading of the beam.

206 The goal of this paper is to determine the amount of reflectivity of the continental slope. This is a hard
 207 number to determine in a complicated geometry, and naturally depends on the region of integration. For
 208 the SHELF configuration the situation is relatively simple, and we use it to illustrate the numerical technique
 209 used below. The signal in the full simulation is assumed to consist of an “incoming” signal and a reflected
 210 signal, so we can decompose the east-west velocity amplitude of the first vertical mode (for example) as:

$$u_1^t(x, y) = u_1^i + u_1^r \quad (8)$$

$$v_1^t(x, y) = v_1^i + v_1^r \quad (9)$$

$$p_1^t(x, y) = p_1^i + p_1^r \quad (10)$$

211 where u_1^t is the complex amplitude of the M_2 , mode-1 east-west velocity of the simulation with the reflection,
 212 u_1^i of the incoming signal, and u_1^r of the reflected signal. We assume for this example that the incoming
 213 signal u_1^i is given by the NO TOPO simulation, and u_1^t is from the SHELF simulation. The reflected signal
 214 u_1^r is simply the difference of these two.

215 In order to compute and energy budget, we consider that the energy fluxes are calculated from the

216 decomposed signals as:

$$P_{u1}^t = u_1^t p_1^t \quad (11)$$

$$= \underbrace{u_1^i p_1^i}_{\text{Incoming}} + \underbrace{u_1^r p_1^r}_{\text{Reflected}} + \underbrace{u_1^i p_1^r + u_1^r p_1^i}_{\text{Cross Terms}} \quad (12)$$

$$P_{v1}^t = v_1^t p_1^t \quad (13)$$

$$= \underbrace{v_1^i p_1^i}_{\text{Incoming}} + \underbrace{v_1^r p_1^r}_{\text{Reflected}} + \underbrace{v_1^i p_1^r + v_1^r p_1^i}_{\text{Cross Terms}} \quad (14)$$

217 The cross terms are not negligible for any realistic forcing, and indeed give rise to the interference patterns
 218 seen above, and is a consequence of rotation's influence on the internal waves (Nash et al. 2004; Martini
 219 et al. 2007).

220 The “total” response (figure 9d) consists of the incoming response (figure 9a), and the “reflected” signal
 221 (figure 9b), and substantial cross-terms (figure 9c). The cross terms are mostly perpendicular to the direction
 222 of reflection (i.e. perpendicular to the shelf) and alternate fluxing energy to the north and south every half
 223 cross-shelf wavelength. Combined, these three components give the “total” flux with net fluxes to the north
 224 in alternating peaks every full offslope wavelength.

225 The reflected response (figure 9b) shows approximately what we would expect with energy being radiated
 226 to the north-east. There is some concentration of this energy at $y \approx 75\text{km}$, and $y \approx 225\text{km}$. As above, this
 227 is because of coupling with a slope wave that is strummed by the initial conditions. This coupling causes
 228 a redistribution of the reflected energy, focusing it approximately every along-slope wavelength of the shelf
 229 wave (we show below that this wavelength changes as the shelf geometry changes).

230 Performing this analysis for the lowest 10 modes, we arrive at an energy budget for the shelf in the green
 231 box in the figures ($0 < y < 400\text{ km}$, and $x < 80\text{ km}$; figure 9, inset budgets). Note that we assume the
 232 flux through $x = 0$ is zero. With this calculation, we see that 408 MW is incident on the shelf in mode-1.
 233 There is also a net flux of 50 MW into this region from the cross terms. This is a redistribution of energy
 234 from north of our box into the box. There is a net convergence of this cross-term energy because there is
 235 dissipation in the box; in a purely inviscid solution this term should balance to zero over a closed box. If we
 236 move the integration further north, the cross-term flux drops to zero.

237 Most of the incoming energy reflects back out of the box (figure 9b), with the bulk remaining in mode 1,
 238 and some scattering to higher modes due to the shelf. This scattered energy reflects to the north east (not
 239 shown). The mode-1 reflection is affected by a shelf wave that transfers energy to and from the barotropic
 240 tide along the slope, resulting in nulls and peaks in the mode-1 reflection.

241 *b. Tasman Rise only*

242 The Tasman Rise has a profound effect on the energy that impacts the continental slope, as well as
243 having some back reflection (figure 8e and f). The incoming beam is almost 500 km wide at $x = 0$ if there is
244 no Tasman Rise, but breaks into three narrower beams when there is a Tasman Rise (figure 8e). Upstream
245 of the rise, the effect is somewhat less energy propagating westward, with an interference pattern towards
246 the east indicating some back reflection.

247 This pattern can be explained in terms of diffraction of the internal tide beam from a deep obstacle (i.e.
248 Johnston and Merrifield 2003). There is a down-wave concentration of energy along the seamount's axis,
249 a null, and sidelobes to the north and south. In this case, the incident beam is of comparable size to the
250 obstacle, leading to an asymmetry, and a stronger lobe to the north than south.

251 Most of the response due to the Tasman Rise can be modeled simply as a cylindrical obstacle in the
252 beam (figure 8b and c). Here our obstacle is 1800 m high in 5000 m of water, and has a radius of 50 km
253 (figure 7). This captures most of the features of the actual Tasman Rise, despite not having a shallow spire
254 in the center and being slightly smaller than the real Rise. The differences make the simplified response
255 have weaker nulls and the whole response is directed a bit further north than the real Rise. Adding the shelf
256 (figure 8c) yields a response that bears substantial similarity to the REAL forcing case.

257 Decomposing into an incoming and reflected signal (figure 10) demonstrates the effect of the Tasman
258 Rise on the response. Less energy is incident on the control volume, largely because the diffraction redirects
259 some of that energy to the north of $y = 400\text{km}$. There is a strong reflection of energy where the main
260 diffraction lobe reflects from the slope (figure 10b), and a smaller maximum just to the north ($y = 250\text{km}$)
261 due to the along-shelf wave that is strummed. There is a reflection further north where the northern lobe of
262 the diffraction pattern reflects.

263 The incoming energy has some more higher mode content due to scattering at the cylindrical rise (fig-
264 ure 10a), though it is still 95% mode-1. The reflection is almost 80% mode-1, with some scattering to higher
265 modes. The net flux shows approximately 15% of the incoming energy is dissipated at the shelf.

266 *c. Real Case*

267 The REAL forcing is similar, if more complex (figure 11). The simulation using the bathymetry in the
268 RISE ONLY case (figure 8e) is used as the "Incoming" energy flux, and the REAL (figure 8f) case is the
269 "Total". Compared to the cylindrical rise, the real Tasman Rise creates a sharper diffraction pattern, and
270 more back reflection. However, the REAL simulation has many of the same features as the RISE AND SHELF
271 simulation (figure 8c).

272 Slightly less incoming energy passes into the control volume (figure 11a) because the diffraction by the
273 real Tasman Rise is sharper than the cylindrical rise. As for the cylindrical rise case, there is some incoming
274 higher mode energy due to forward scattering, though again over 95% is mode-1. Reflection is concentrated
275 near $y = 125$ km and $y = 450$ km, associated with the diffraction nodes, with about 85% in mode 1
276 (figure 11b). Dissipation is less than 25% of the incoming energy (figure 11d).

277 5. Discussion

278 a. Scattering from linear calculations

279 The fraction of reflected tide can be predicted from linear theory to relatively good approximation using
280 the method described by Kelly et al. (2013b) of matching Laplacian tidal solutions at discrete steps on a
281 discretized topography. Their work originally only considered tides normally incident to the topography, but
282 oblique incidence is straight forward to calculate using the same numerical method, taking into account that
283 the wavenumber normal to the topography is given by $k = K \cos \theta$. Oblique incidence makes a substantial
284 difference in the modal distribution of the reflected tide, with more oblique reflections scattering less energy
285 to higher modes for the topography used in the SHELF case (figure 12). At normal incidence for this shelf
286 shape and stratification 75% of the incoming energy reflects as mode 1, whereas for 30° incidence, it is closed
287 to 85%, and reaches almost 100% as incidence increases. Agreement between the full numerical simulation
288 and the linear model is good, though there is less energy in mode 2 and more in mode 3 in the model than
289 the linear prediction. Interestingly, most of this increased mode-1 reflection is at the expense of mode-2.

290 Linear reflection from the real topography is quite variable, depending on the two-dimensional topography
291 chosen and the angle of incidence (figure 13). Note that as the angle of incidence increases the standing wave's
292 horizontal wavelength in the x direction increases. However also note that high mode reflected response has
293 the same x direction wavelength. The response at $y = 240$ km goes through a significant scattering into
294 higher modes and dissipation, with only 28% of incoming mode-1 energy reflecting as mode-1. Interestingly
295 this number drops dramatically as the incident angle increases from 30 to 60 degrees.

296 The variability of reflectivity along the slope is considerable (figure 14), with values ranging from 9% to
297 96%. However, much of the slope where the diffracted energy is the strongest ($y \approx 125$ km and $y \approx 425$ km) is
298 also where the incoming energy in the means is the strongest, so when weighted by the forcing we expect the
299 overall reflectivity to be approximately 80%. In the REAL numerical run, the reflectivity into mode-1 is only
300 about 67%, so somewhat less. The differences are likely due to dissipation and possibly three dimensionality
301 of the reflection pattern.

302 b. Comparison with Glider Antennas

303 Gliders surveys at this site are described by Johnston et al. (2015). First, the gliders saw a substantial
304 concentration of energy shoreward of the Tasman Rise. This is a feature of the model, and clearly explained
305 by the diffraction of energy by the Tasman Rise (figure 11).

306 For the region in the lee of the Tasman Rise, Johnston et al. (2015) estimate a reflectivity of the mode-1
307 internal tide of between 0.8 to 1.0 by fitting plane waves to the velocity and displacement amplitudes and
308 phases. If we confine our incoming versus outgoing energy budget to the region $80 \text{ km} < y < 200 \text{ km}$,
309 representative of their *Spray 56* deployment, we calculate a reflectivity of 0.7, which is lower than their
310 lowest estimate of 0.8, and much lower than their high estimate of 1.0. Their *Spray 55* deployment covered
311 more of the slope (up to $y = 300 \text{ km}$). In this domain, they estimate a reflectivity of 0.6. This is in excellent
312 agreement with the numerical simulation, which achieves exactly the same result from $0 \text{ km} < y < 300 \text{ km}$.

313 The directions of wave propagation fit from the glider data is not as well in agreement with the model.
314 The fits to the *Spray 55* data show incoming energy at between 125 and 145 degrees, which is similar to
315 the model. However the reflection is slightly south of due east (0 to -30 degrees geographic), whereas the
316 numerical model is definitely to the north east far from shore. An explanation is evident from close inspection
317 of figure 11b between the Tasman Rise and the continental slope. Here the off-shore energy flux is almost
318 exactly in the x-direction, (-12 degrees geographic), in agreement with the glider observations.

319 Finally, one of the gliders (*Spray 56*) picked out a northward propagating disturbance along the conti-
320 nental slope with wavelength of 100 km. This wavelength matches the wavelength of the slope wave seen in
321 the real simulations (figure 5a,b). Interestingly, they only pick this wavelength out in vertical displacement
322 data, not in velocity.

323 c. Slope wave importance and dynamics

324 The structure of the barotropic-to-baroclinic conversion on the slope is an intriguing feature of these
325 simulations. It shows up most clearly in the SHELF simulations because of the simplified bathymetry.
326 However, it is also clear in the REAL simulation (figure 5a). This slope wave redistributes energy in the
327 reflected baroclinic response (figure 9), taking a relatively homogenous incoming energy source and focusing
328 the reflection every 200 km or so along shelf.

329 This wave is a slope mode that is strummed by the incident internal tide at the “corner” of the topography
330 ($x = 0, y = 0$); a long shelf without the corner does not excite this wave, nor does an internal tide
331 coming directly from the east and hitting the topography at a normal angle. The along-slope wavelength is
332 independent of the along-slope wavelength in the open water (tested by changing the angle of the incident

333 tide), and is a robust feature of the shelf shape. Wider shelves have shorter along-slope wavelengths, and
334 narrow shelves have longer (figure 15).

335 These waves are superinertial, and hence not traditional subinertial coastally trapped waves (i.e. Brink
336 1991). However, Dale and Sherwin (1996) show that superinertial waves on continental slopes can still have
337 modes that grow more rapidly in frequency and along-slope wavenumber. Here our frequency is fixed, so we
338 expect there to be resonant along-slope wavenumbers. The vertical-cross slope response of these waves, or
339 modes, are basically a local mode-1 in the deep ocean, and close to barotropic on the shallow shelf, matching
340 our findings here.

341 These slope modes transfer energy from the mode-1 internal tide to the barotropic (in our local account-
342 ing). Because the waves are super-inertial, they are not perfectly trapped on the slope, and require forcing to
343 keep their energy, and re-radiate energy offshore. Calculating how much energy is redistributed as a function
344 of the shelf-wave amplitude is an interesting problem that will require further research.

345 6. Summary

346 A mode-1 internal tide was launched at a variety of topographies representing the Tasmanian continental
347 slope. The goal was to determine the “reflectivity” of this slope, in terms of the modal content of the
348 reflected energy and the local dissipation. The latter is somewhat suspect in this model because of crude
349 lateral resolution, but the REAL simulation indicated that 21% of the incoming energy was dissipated, and
350 65% was reflected as mode-1 energy. The incoming internal tide flux used here was weak compared to the
351 flux modeled and inferred from altimetry in the Tasman Sea, so we expect the dissipation in more strongly
352 forced models to increase.

353 Despite a relatively simple incoming internal tide which is linear, semi-diurnal, and mode-1, we have
354 found a rich and complex response of the topography when the remote wave impacts the topography east
355 of Tasmania. The response can be characterized as follows:

- 356 • Diffraction of the beam by the Tasman Rise,
- 357 • oblique reflection from the continental slope,
- 358 • and a forced slope wave response that redistributes reflected internal energy along-slope.

359 Of these, perhaps only the second effect was expected before carrying out the simulations. However, as we
360 saw above, even the reflection problem is significantly complicated in the presence of three-dimensionality,
361 such that it is difficult to determine the appropriate slope for the incoming wave to impact the shelf.

362 Diffraction around underwater topography should have been expected, however, the relative depth of
363 the obstacle makes it surprising that the effect is so strong. The fact that the size of the Tasman Rise is
364 close to that of a wavelength of the incoming internal tide makes predicting the diffraction pattern difficult.
365 Baines (2007) considers generation of internal tides at seamounts, but does not deal with scattering and
366 diffraction. The problem is similar to electromagnetic waves passing through a wire, but a linear response
367 for that problem is not trivial to compute (i.e. Bonod et al. 2005), and still does not have a confined vertical
368 mode structure as we find in the internal wave problem.

369 The excitation of slope waves is a nice corroboration of theory by Dale et al. (2001), and it has a low-order
370 effect on the redistribution of energy along slope. If the dissipation in this crude model is to be believed (and
371 we feel it is actually close, based on higher resolution runs), the redistribution affects where high dissipation
372 is found (figure 5). Finally, it adds more inhomogeneity to the reflected internal tide.

373 The complexity grows if other real-world influences are to be accounted for. The East Australian Current
374 flows along this slope, varying the stratification in the horizontal, provides lateral shears that can distort the
375 internal tide response, and carrying eddies that can add a strong time dependence to these effects. Even in
376 two dimensions, the strength of the internal tide reflection can be significantly impacted by the phase of the
377 incoming tide with other baroclinic modes Klymak et al. (2011) or the barotropic (Kelly and Nash 2010). The
378 simulations here exclude the local barotropic tide, so this would certainly complicate the reflected response.
379 Finally, the internal tide used here was monotonic, whereas the real tide will have other frequencies, most
380 notably subinertial diurnal frequencies that will have trapped wave responses (personal communication, R.
381 Musgrave).

382 Regardless, it is useful to have separated the “simplest” response we could in this system to tease apart the
383 dominant physics. This response is complex enough as it is that it should be clear that solely observational
384 efforts to balance a reflection budget are going to be a challenge. Merging simulations and observations is a
385 likely way forward in understanding the wave field in this complex slope region.

386 *Acknowledgments.*

387 Start acknowledgments here.

REFERENCES

- 390 Baines, P. G., 2007: Internal tide generation by seamounts. *Deep Sea Res. I*, **54 (9)**, 1486 – 1508, doi:
 391 <http://dx.doi.org/10.1016/j.dsr.2007.05.009>, URL <http://www.sciencedirect.com/science/article/pii/S0967063707001306>.
- 393 Bonod, N., E. Popov, and M. Nevière, 2005: Differential theory of diffraction by finite cylindrical objects.
 394 *JOSA A*, **22 (3)**, 481–490.
- 395 Boyer, T., et al., 2013: *World Ocean Database 2013*. NOAA Atlas NESDIS 72, doi:10.7289/V5NZ85MT.
- 396 Brink, K., 1991: Coastal-trapped waves and wind-driven currents over the continental shelf. *Annu. Rev. Fluid Mech.*, **23**, 389–412.
- 398 Buijsman, M. C., et al., 2014: Three-dimensional double-ridge internal tide resonance in Luzon Strait. *J. Phys. Oceanogr.*, **44 (3)**, 850–869.
- 400 Carter, G., et al., 2008: Energetics of M 2 Barotropic-to-Baroclinic Tidal Conversion at the Hawaiian Islands.
 401 *Journal of Physical Oceanography*, **38 (10)**, 2205–2223.
- 402 Dale, A. C., J. M. Huthnance, and T. J. Sherwin, 2001: Coastal-trapped waves and tides at near-inertial
 403 frequencies. *J. Phys. Oceanogr.*, **31 (10)**, 2958–2970.
- 404 Dale, A. C. and T. J. Sherwin, 1996: The extension of baroclinic coastal-trapped wave theory to superinertial
 405 frequencies. *J. Phys. Oceanogr.*, **26 (11)**, 2305–2315.
- 406 Johnston, T. M. S., D. L. Rudnick, and S. M. Kelly, 2015: Standing internal tides in the Tasman Sea
 407 observed by gliders, doi:<http://www-pord.ucsd.edu/~shaunj/files/standing20150528.pdf>, in press *J. Phys. Oceanogr.*
- 409 Johnston, T. S. and M. A. Merrifield, 2003: Internal tide scattering at seamounts, ridges, and islands. *J. Geophys. Res.*, **108 (C6)**, 3180, doi:10.1029/2002JC01528.
- 411 Kang, D., 2011: Barotropic and baroclinic tidal energy. Ph.D. thesis, Stanford University.
- 412 Kang, D. and O. Fringer, 2012: Energetics of barotropic and baroclinic tides in the monterey bay area. *J. Phys. Oceanogr.*, **42 (2)**, 272–290.

- 414 Kelly, S. and J. Nash, 2010: Internal-tide generation and destruction by shoaling internal tides. *Geophysical*
415 *Research Letters*, **37**, L23 611.
- 416 Kelly, S. M., N. L. Jones, and J. D. Nash, 2013a: A coupled model for laplace's tidal equations in a fluid
417 with one horizontal dimension and variable depth. *Journal of Physical Oceanography*, **(2013)**.
- 418 Kelly, S. M., N. L. Jones, and J. D. Nash, 2013b: A coupled model for laplace's tidal equations in a
419 fluid with one horizontal dimension and variable depth. *Journal of Physical Oceanography*, **(2013)**, doi:
420 10.1175/JPO-D-12-0147.1.
- 421 Klymak, J., M. Alford, R. Pinkel, R. Lien, Y. Yang, and T. Tang, 2011: The breaking and scattering of the
422 internal tide on a continental slope. *J. Phys. Oceanogr*, **41**, 926–945, doi:10.1175/2010JPO4500.1.
- 423 Klymak, J. M. and S. M. Legg, 2010: A simple mixing scheme for models that resolve breaking internal
424 waves. *Ocean Modell.*, **33 (3-4)**, 224 – 234, doi:10.1016/j.ocemod.2010.02.005.
- 425 Klymak, J. M., et al., 2006: An estimate of tidal energy lost to turbulence at the Hawaiian Ridge. *J. Phys.*
426 *Oceanogr.*, **36**, 1148–1164.
- 427 Legg, S. and J. M. Klymak, 2008: Internal hydraulic jumps and overturning generated by tidal flow over a
428 tall steep ridge. *J. Phys. Oceanogr.*, **38 (9)**, 1949–1964.
- 429 Marshall, J., E. Shuckburgh, H. Jones, and C. Hill, 2006: Estimates and implications of surface eddy
430 diffusivity in the Southern Ocean derived from tracer transport. *J. Phys. Oceanogr.*, **36 (9)**, 1806–1821.
- 431 Martini, K., M. Alford, J. Nash, E. Kunze, and M. Merrifield, 2007: Diagnosing a partly standing internal
432 wave in Mamala Bay, Oahu. *Geophys. Res. Lett.*, **34 (17)**, L17 604.
- 433 Martini, K. I., M. H. Alford, E. Kunze, S. M. Kelly, and J. D. Nash, 2013: Internal bores and breaking
434 internal tides on the oregon continental slope. *J. Phys. Oceanogr.*, **43**, 120–139.
- 435 Melet, A., R. Hallberg, S. Legg, and K. Polzin, 2013: Sensitivity of the ocean state to the vertical distribution
436 of internal-tide-driven mixing. *J. Phys. Oceanogr.*, **43 (3)**, 602–615.
- 437 Mercier, M. J., N. B. Garnier, and T. Dauxois, 2008: Reflection and diffraction of internal waves analyzed
438 with the Hilbert transform. *Phys. Fluids*, **20 (8)**, 086 601.
- 439 Nash, J., M. Alford, E. Kunze, K. Martini, and S. Kelley, 2007: Hotspots of deep ocean mixing on the
440 Oregon continental slope. *Geophys. Res. Lett.*, **34**, L01 605, doi:10.1029/2006GL028 170.

- 441 Nash, J. D., E. Kunze, J. M. Toole, and R. W. Schmitt, 2004: Internal tide reflection and turbulent mixing
442 on the Continental Slope. *J. Phys. Oceanogr.*, 1117–1134.
- 443 Polzin, K. L., 2009: An abyssal recipe. *Ocean Modelling*, **30** (4), 298–309, doi:doi:10.1016/j.ocemod.2009.
444 07.007.
- 445 Rainville, L., T. Johnston, G. S. Carter, M. A. Merrifield, R. Pinkel, P. F. Worcester, and B. D. Dushaw,
446 2010: Interference pattern and propagation of the m2 internal tide south of the hawaiian ridge. *J. Phys.*
447 *Oceanogr.*, **40** (2).
- 448 Smith, W. and D. Sandwell, 1997: Global sea floor topography from satellite altimetry and ship depth
449 soundings. *Science*, **277** (5334), 1956.
- 450 St. Laurent, L. and C. Garrett, 2002: The role of internal tides in mixing the deep ocean. *J. Phys. Oceanogr.*,
451 **32**, 2882–2899.
- 452 Whiteway, T., 2009: Australian bathymetry and topography grid, june 2009. scale 1:5000000. Tech. rep.,
453 Geoscience Australia, Canberra. doi:10.4225/25/53D99B6581B9A.
- 454 Zhao, Z. and M. H. Alford, 2009: New altimetric estimates of mode-1 M2 internal tides in the central North
455 Pacific Ocean. *J. Phys. Oceanogr.*, **39** (7), 1669–1684.

456 List of Figures

- 457 1 Schematic of the difficulty of quantifying reflecting fluxes in an inhomogeneous environment.
458 Plane waves are trivial. Inhomogeneous incoming waves or reflections are significantly more
459 difficult. 21
- 460 2 Location of TTide experiment: a) Energy flux in a regional numerical simulation. Color is
461 the absolute value of the flux, arrows its direction. The magenta box indicates the numerical
462 modeling domain used in this paper. b) Detail of the bathymetry on the Tasman slope. The
463 magenta lines indicate 100 km in the x-direction, and 300 km in the y direction in the modeling
464 domain used in this paper. 22
- 465 3 a) Forcing used to drive the models used in this paper. Two mode-1 internal wave sources
466 are located to the south east (blue lines). The model domain is rotated 12 degrees from
467 geographic so the shelf break approximately lies along $x = 0$. Typical model domain and
468 sponge region is indicated as green rectangles. The 250, and 3000-m isobaths are contoured.
469 Arrows show the direction of the energy flux, and are scaled by its strength. b) Energy flux
470 of analytical response of energy reflecting from a wall at $x = 0$, north of $y = 0$. c) Phase of
471 reflected response. 23
- 472 4 a)-d) Surface x-direction velocity for four snapshots. a) is the initial conditions (slightly
473 modified after a tidal cycle) and d) is the steady state. Grey contours are depths at 3000,
474 2000, 1000, and 250-m. e)-h) is depth-integrated baroclinic energy flux at the same time
475 periods, with arrows indicating direction. 24
- 476 5 Energy budget over the 19th tidal cycle of a) Barotropic to baroclinic conversion; b) Baro-
477 clinic energy flux convergence ($-\nabla F_{bc}$); c) rate of change of baroclinic energy; d) residual
478 representing the dissipation in the model $D = -\nabla \mathbf{F}_{bc} + \text{Conv.} - dE/dt$. The green box is the
479 region for the energy time series (figure 6b). 25

480 6 a) Integral in x to 80 km offshore of the energy terms in figure 5 for the REAL case. Note
481 that the barotropic-baroclinic term (red) is of the same order as the baroclinic convergence
482 (cyan) and the residual dissipation (gray) for most of the shelf. b) Energy budget time series
483 for the “Real” case, tidally averaged, where time is normalized by $T = 12.4h$, between $y = 0$
484 to $y = 400$ km. There is still a small residual increase in the energy with time (purple),
485 representing the accumulation of high-mode energy in the region. Net barotropic-baroclinic
486 conversion (red) is small and negative, indicating a small net loss to the barotropic tide in
487 this region. The bulk of the budget is the balance between baroclinic flux convergence (blue)
488 and the residual “dissipation” (gray). c) Net flux in the box defined by $0 < x < 80$ km, and
489 $0 < y < 400$ km. Green is the value for the net flux (no modal decomposition). Blue bars are
490 the modal decomposition. There is a net incoming flux in mode 1 and net reflecting fluxes in
491 higher modes (primarily modes 2-4). 26

492 7 Cross sections of topographies from $y = 50$ km. 27

493 8 Energy flux for six geometries at tidal cycle 20. Grey depth contours are -3000, -2000, -1000
494 and -250 m. Arrows indicate the direction of energy flux. See figure 7 for bathymetry cross
495 sections at $y = 50$ km. 28

496 9 Mode-1 decomposition of energy fluxes for the SHELF experiment. a) Incoming energy flux
497 calculated from the NO TOPO simulation (figure 8a). Note that the shelf bathymetry is
498 contoured on this plot (grey lines, and green “land”), but this bathymetry was not part
499 of this simulation. The green line demarks the region the energy budget in the inset was
500 integrated over. The green diamonds are the location of a synthetic mooring, and the arrow
501 indicates the estimated incoming flux from a plane wave fit over the three moorings of the
502 “Total” simulation (see text). b) Reflected energy flux calculated from the difference between
503 the velocities and displacements of the Total simulation (panel d) and the “Incoming” (panel
504 a). Blue arrow is the outgoing flux from a plane wave fit over the mooring array from the
505 “Total” simulation. c) Energy flux cross terms between the incoming and outgoing waves. d)
506 Total simulation from the SHELF case (figure 8d) 29

507 10 Mode-1 decomposition of energy fluxes for the RISE-SHELF experiment. 30

508 11 Energy decomposition based on taking the NO TOPO case as the incoming wave, and RISE
509 as the total wavefield and looking at the energy flux of the difference between their waves
510 (reflected wave field) and the energy flux associated with the cross terms between. 31

511 12 The reflected flux for the SHELF bathymetry (diamonds), and the results of a linear internal
512 tide solution through a series of incident mode-1 angles. 32

- 513 13 Velocity snapshots from linear calculation of reflecting mode-1 internal tide from three sections
514 of bathymetry, and three incident angles. 33

515 14 Strength of the reflection calculated from the two-dimensional linear method assuming an
516 incident angle of 30 degrees, divided into vertical modes. Dashed lines are means of mode-
517 1 reflection, centered where the main and northern lobes of the diffraction pattern hit the
518 bathymetry, and one from $y = 0$ km to $y = 400$ km. Compare the reflectivity here with the
519 67% reflectivity of mode 1 in the REAL simulation (figure 11). 34

520 15 Barotropic to baroclinic conversion for different shelf widths from widest (a) to narrowest (d).
521 Arrows are barotropic flux vectors. Note how the along-slope barotropic flux is almost entirely
522 confined to conversion dipoles along slope. 35

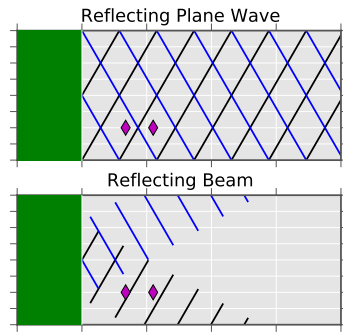


FIG. 1. Schematic of the difficulty of quantifying reflecting fluxes in an inhomogeneous environment. Plane waves are trivial. Inhomogeneous incoming waves or reflections are significantly more difficult.

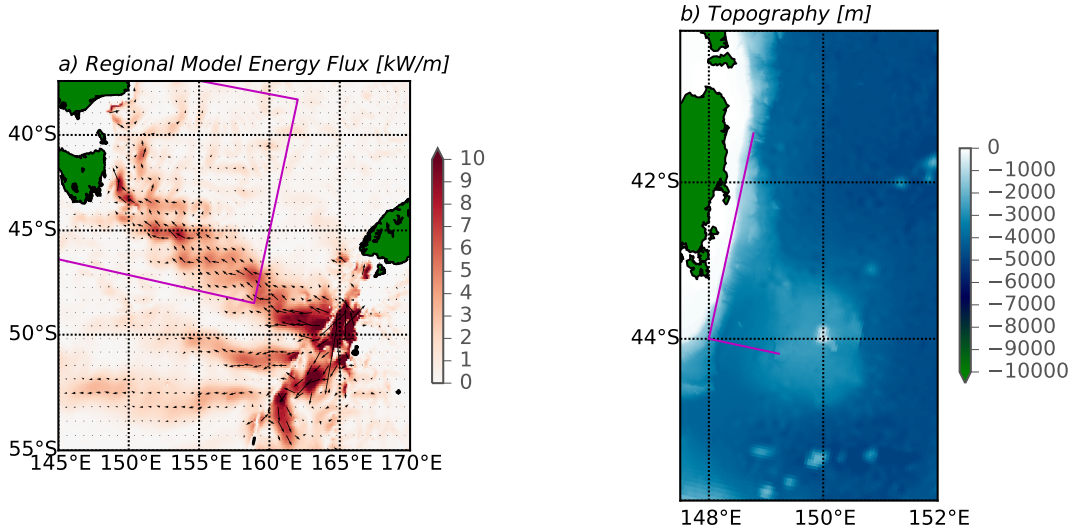


FIG. 2. Location of TTide experiment: a) Energy flux in a regional numerical simulation. Color is the absolute value of the flux, arrows its direction. The magenta box indicates the numerical modeling domain used in this paper. b) Detail of the bathymetry on the Tasman slope. The magenta lines indicate 100 km in the x-direction, and 300 km in the y direction in the modeling domain used in this paper.

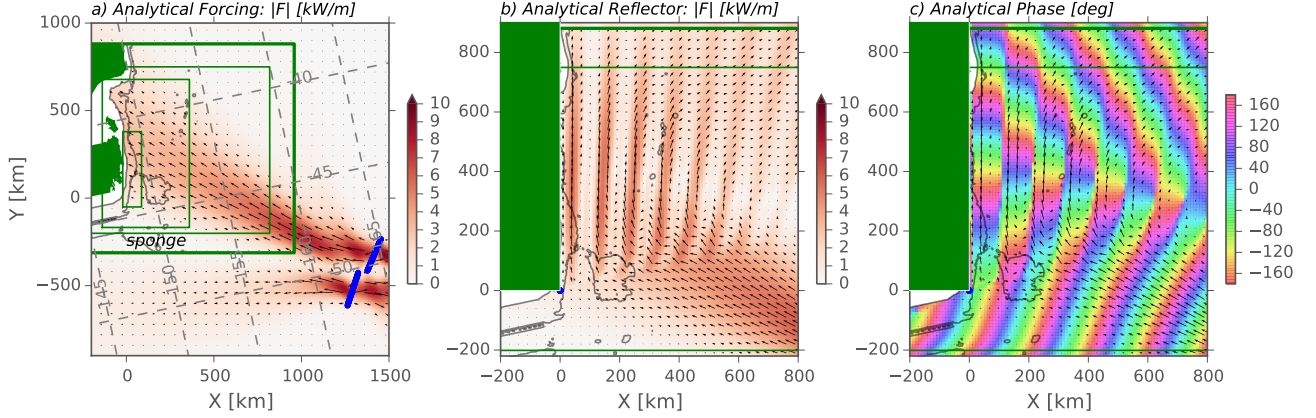


FIG. 3. a) Forcing used to drive the models used in this paper. Two mode-1 internal wave sources are located to the south east (blue lines). The model domain is rotated 12 degrees from geographic so the shelf break approximately lies along $x = 0$. Typical model domain and sponge region is indicated as green rectangles. The 250, and 3000-m isobaths are contoured. Arrows show the direction of the energy flux, and are scaled by its strength. b) Energy flux of analytical response of energy reflecting from a wall at $x = 0$, north of $y = 0$. c) Phase of reflected response.

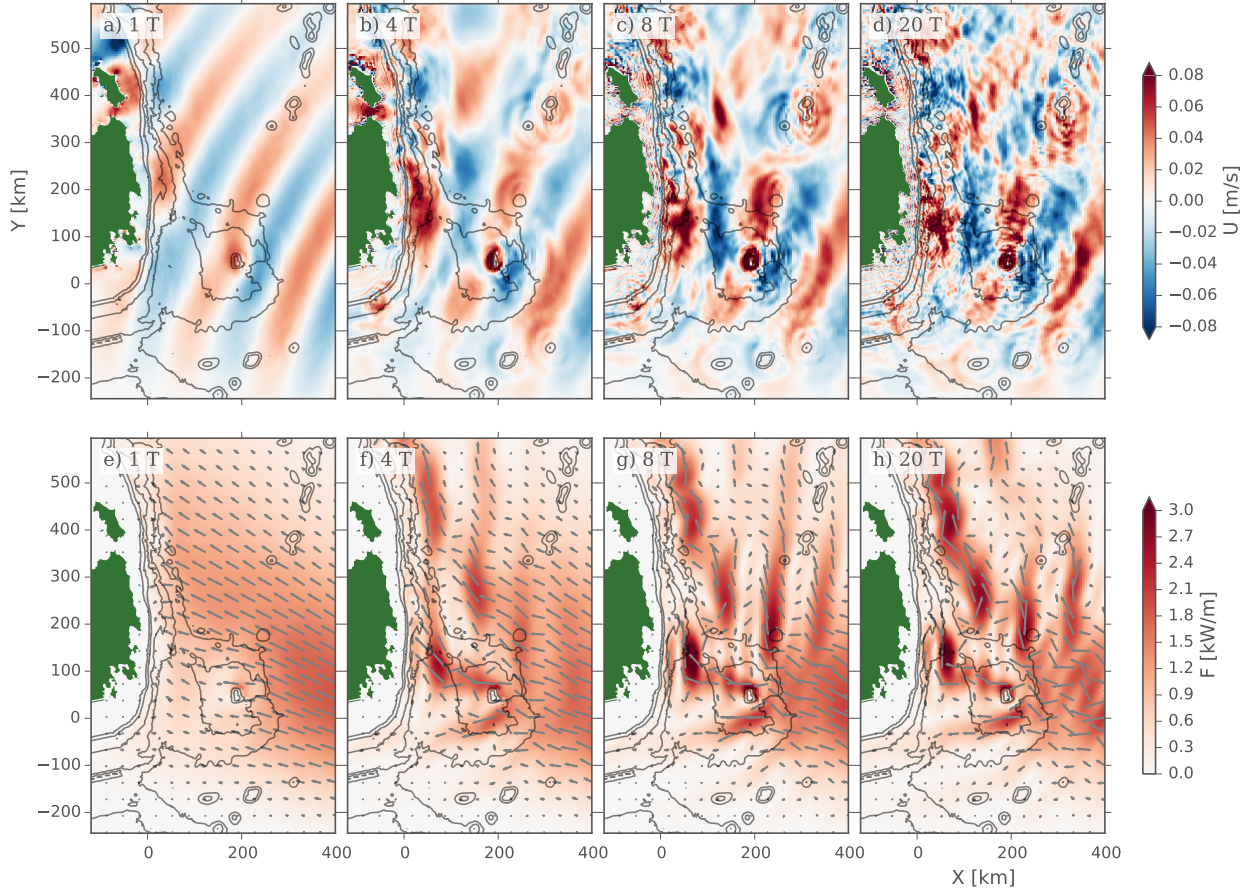


FIG. 4. a)-d) Surface x-direction velocity for four snapshots. a) is the initial conditions (slightly modified after a tidal cycle) and d) is the steady state. Grey contours are depths at 3000, 2000, 1000, and 250-m. e)-h) is depth-integrated baroclinic energy flux at the same time periods, with arrows indicating direction.

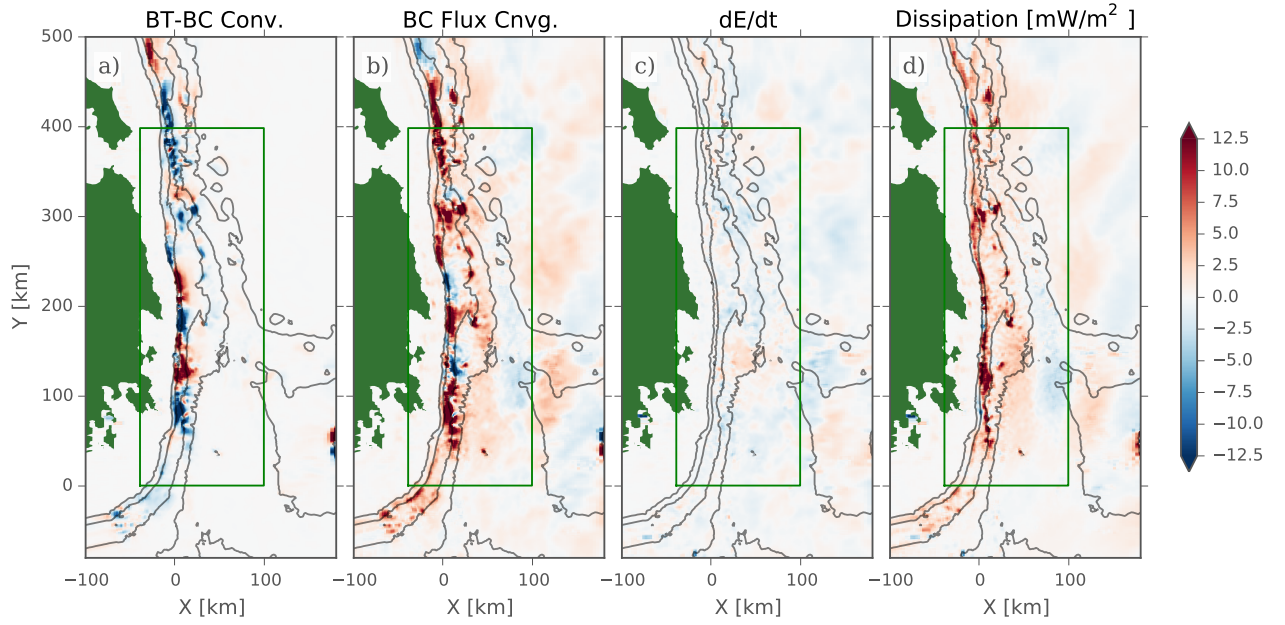


FIG. 5. Energy budget over the 19th tidal cycle of a) Barotropic to baroclinic conversion; b) Baroclinic energy flux convergence ($-\nabla F_{bc}$); c) rate of change of baroclinic energy; d) residual representing the dissipation in the model $D = -\nabla F_{bc} + \text{Conv.} - dE/dt$. The green box is the region for the energy time series (FIG. 6b).

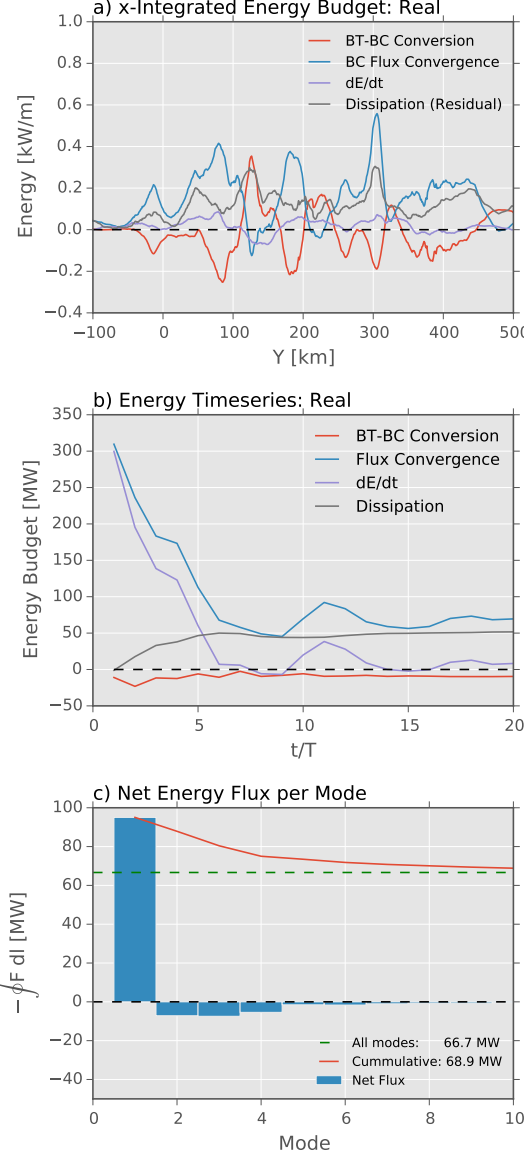


FIG. 6. a) Integral in x to 80 km offshore of the energy terms in FIG. 5 for the REAL case. Note that the barotropic-baroclinic term (red) is of the same order as the baroclinic convergence (cyan) and the residual dissipation (gray) for most of the shelf. b) Energy budget time series for the “Real” case, tidally averaged, where time is normalized by $T = 12.4h$, between $y = 0$ to $y = 400$ km. There is still a small residual increase in the energy with time (purple), representing the accumulation of high-mode energy in the region. Net barotropic-baroclinic conversion (red) is small and negative, indicating a small net loss to the barotropic tide in this region. The bulk of the budget is the balance between baroclinic flux convergence (blue) and the residual “dissipation” (gray). c) Net flux in the box defined by $0 < x < 80$ km, and $0 < y < 400$ km. Green is the value for the net flux (no modal decomposition). Blue bars are the modal decomposition. There is a net incoming flux in mode 1 and net reflecting fluxes in higher modes (primarily modes 2-4).

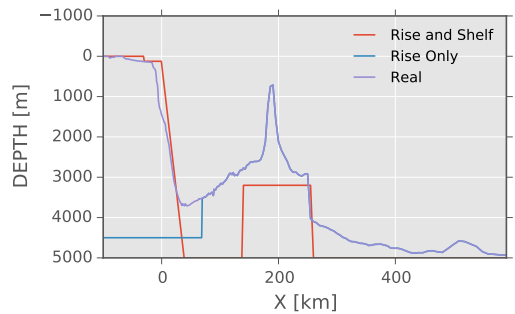


FIG. 7. Cross sections of topographies from $y = 50$ km.

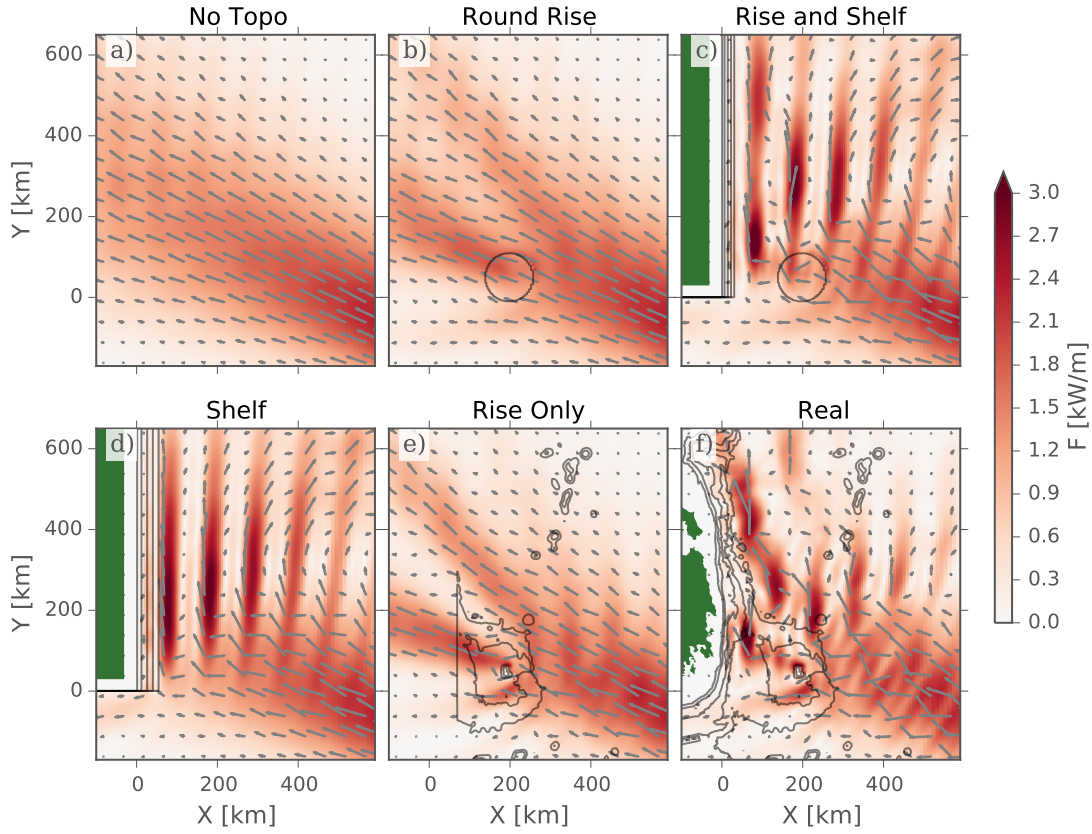


FIG. 8. Energy flux for six geometries at tidal cycle 20. Grey depth contours are -3000, -2000, -1000 and -250 m. Arrows indicate the direction of energy flux. See FIG. 7 for bathymetry cross sections at $y = 50$ km.

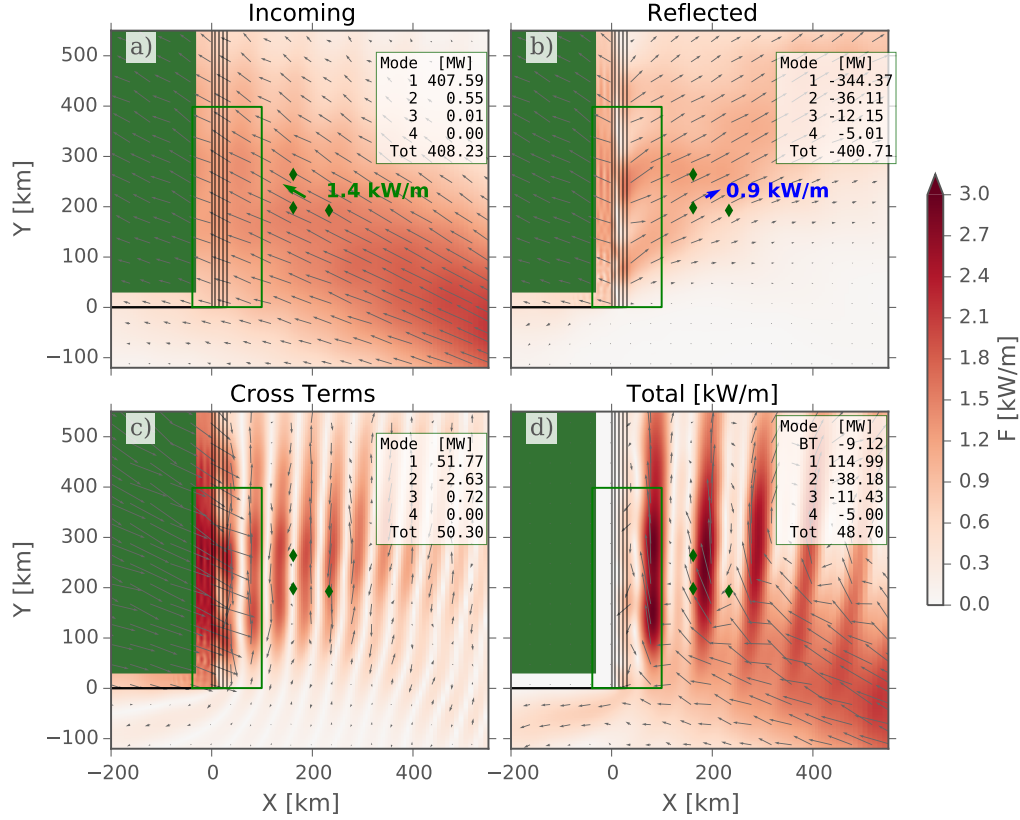


FIG. 9. Mode-1 decomposition of energy fluxes for the SHELF experiment. a) Incoming energy flux calculated from the NO TOPO simulation (FIG. 8a). Note that the shelf bathymetry is contoured on this plot (grey lines, and green “land”), but this bathymetry was not part of this simulation. The green line marks the region the energy budget in the inset was integrated over. The green diamonds are the location of a synthetic mooring, and the arrow indicates the estimated incoming flux from a plane wave fit over the three moorings of the “Total” simulation (see text). b) Reflected energy flux calculated from the difference between the velocities and displacements of the Total simulation (panel d) and the “Incoming” (panel a). Blue arrow is the outgoing flux from a plane wave fit over the mooring array from the “Total” simulation. c) Energy flux cross terms between the incoming and outgoing waves. d) Total simulation from the SHELF case (FIG. 8d)

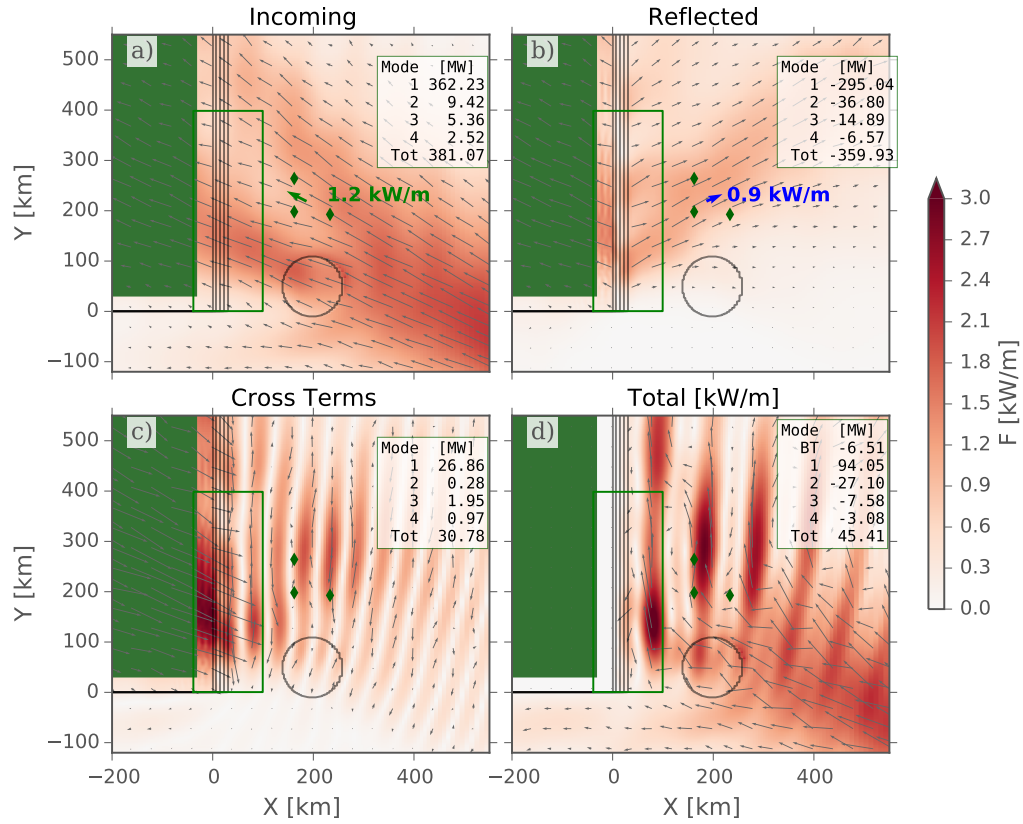


FIG. 10. Mode-1 decomposition of energy fluxes for the RISE-SHELF experiment.

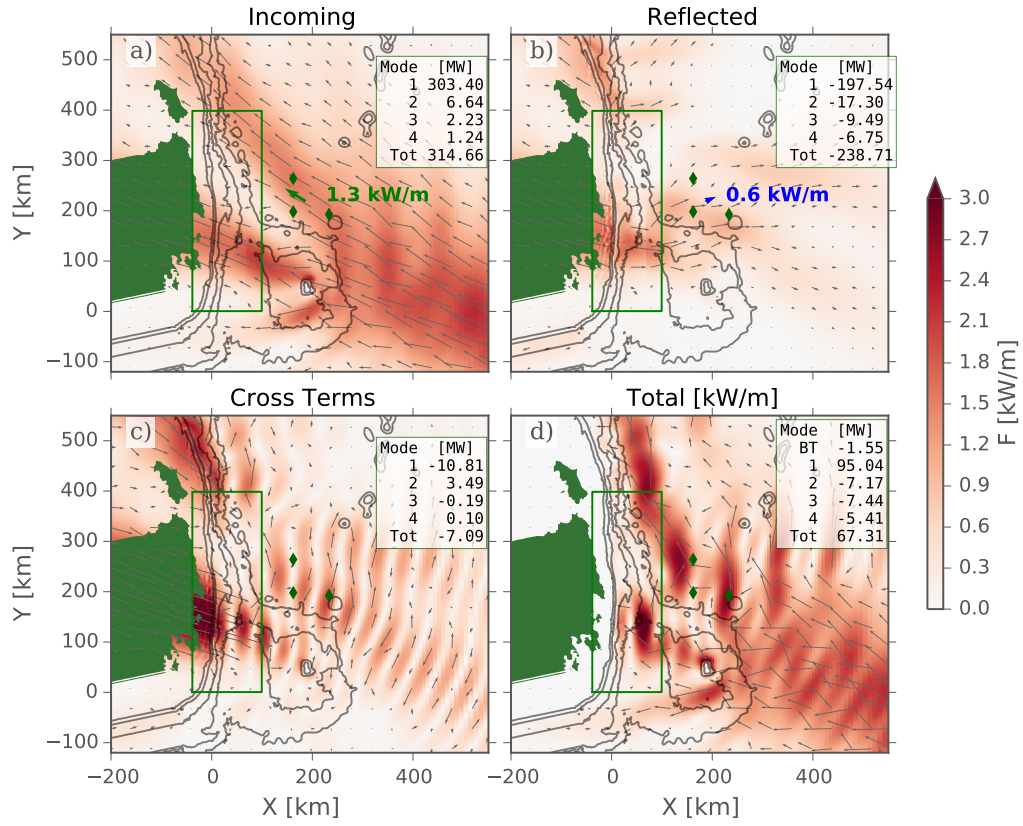


FIG. 11. Energy decomposition based on taking the No TOPO case as the incoming wave, and RISE as the total wavefield and looking at the energy flux of the difference between their waves (reflected wave field) and the energy flux associated with the cross terms between.

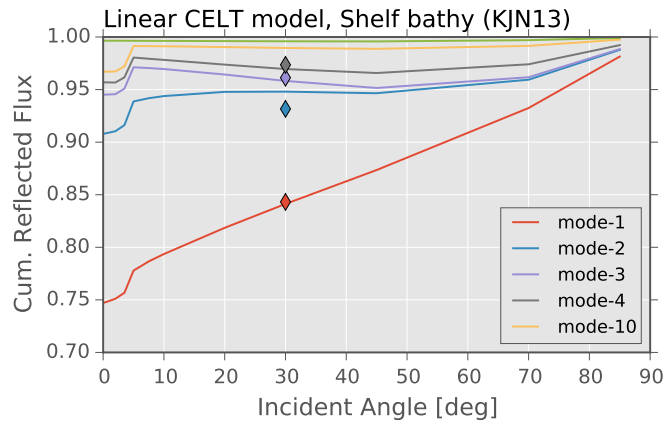


FIG. 12. The reflected flux for the SHELF bathymetry (diamonds), and the results of a linear internal tide solution through a series of incident mode-1 angles.

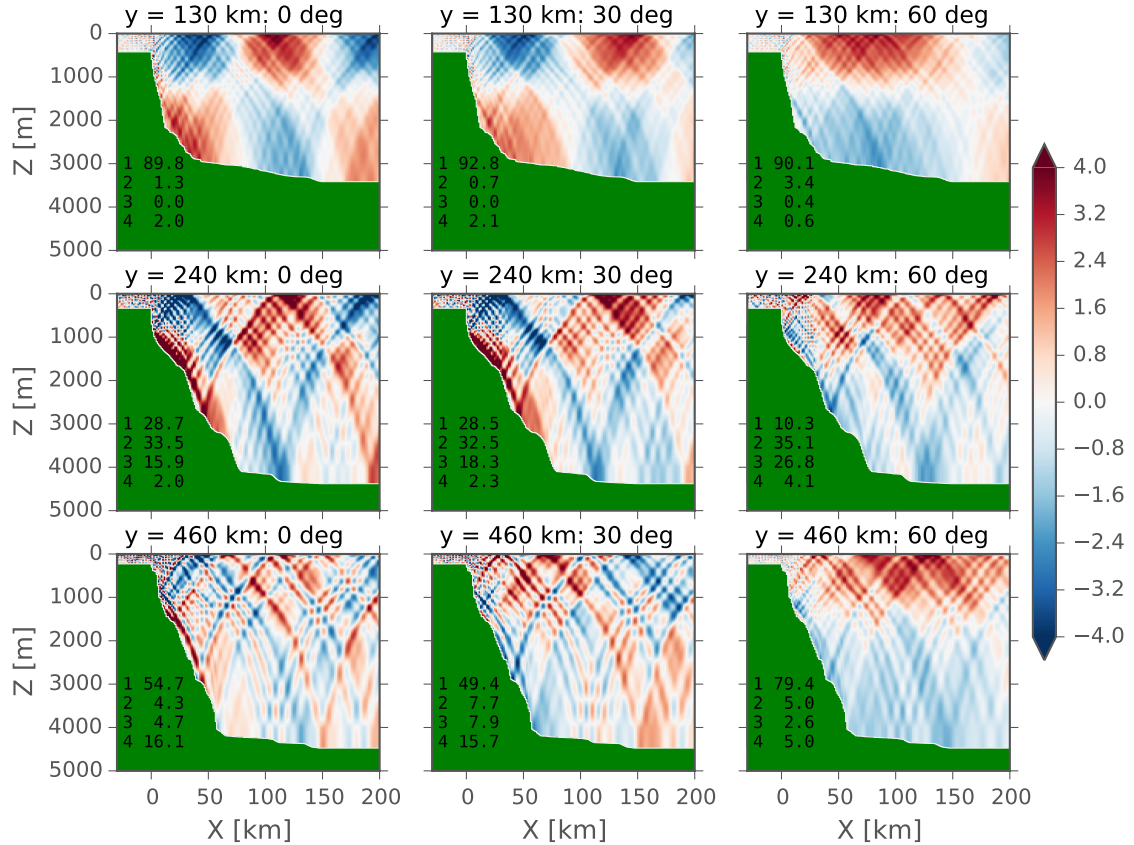


FIG. 13. Velocity snapshots from linear calculation of reflecting mode-1 internal tide from three sections of bathymetry, and three incident angles.

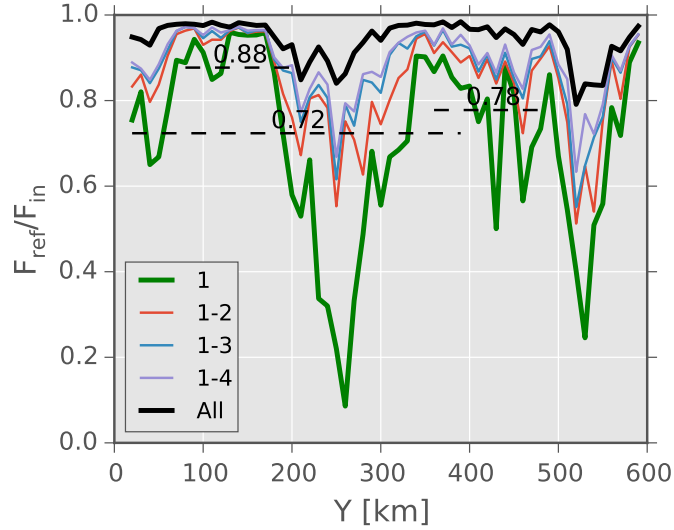


FIG. 14. Strength of the reflection calculated from the two-dimensional linear method assuming an incident angle of 30 degrees, divided into vertical modes. Dashed lines are means of mode-1 reflection, centered where the main and northern lobes of the diffraction pattern hit the bathymetry, and one from $y = 0 \text{ km}$ to $y = 400 \text{ km}$. Compare the reflectivity here with the 67% reflectivity of mode 1 in the REAL simulation (FIG. 11).

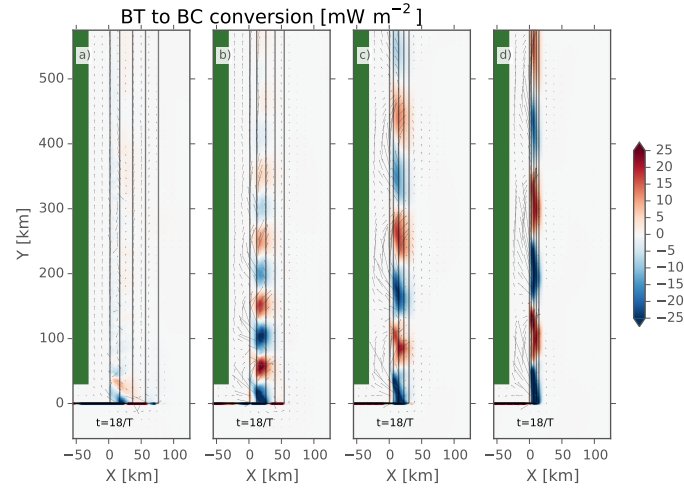


FIG. 15. Barotropic to baroclinic conversion for different shelf widths from widest (a) to narrowest (d). Arrows are barotropic flux vectors. Note how the along-slope barotropic flux is almost entirely confined to conversion dipoles along slope.